JPE 19-3-8

https://doi.org/10.6113/JPE.2019.19.3.691
ISSN(Print): 1598-2092 / ISSN(Online): 2093-4718

Transition Control of Standby and Operation Modes of Wireless Charging System for Inspection Robots

Han Liu[*,**], Linlin Tan[*,**], Xueliang Huang[†,*,**], and Dariusz Czarkowski[***]

[†,*]School of Electrical Engineering, Southeast University, Nanjing, China
[**]Key Laboratory of Smart Grid Technology and Equipment in Jiangsu Province, Zhenjiang, China
[***]Department of Electrical and Computer Engineering, NYU Tandon School of Engineering, Brooklyn, NY, USA

Abstract

To solve the problems in the contact charging of inspection robots, a wireless charging system for inspection robots and a control strategy are introduced in this paper. Circuit models of a wireless power system with a compound compensation circuit and a three-phase Class-D resonant inverter are set up based on circuit theory. An output voltage control method based on the equal spread regulation of the phase difference between adjacent phases and the parameter correction method in the primary compound compensation circuit are proposed. The dynamic characteristics of the key parameters varying with the secondary coil position are obtained to further investigate the adaptive location scheme during the access and exit processes of moving robots. Combining the output voltage control method and the adaptive location scheme, a transition control strategy for the standby and operation modes of the wireless charging systems for inspection robots is put forward to realize the system characteristics including the low standby power in the standby mode and the high receiving power in the operation mode. Finally, experiments are designed and conducted to verify the correctness of the theoretical research.

Key words: Adaptive location scheme, Inspection robot, Standby and operation modes, Transition control strategy, Wireless power transmission

I. INTRODUCTION

An inspection robot, a special kind of industrial robot, is usually used in smart factories and substations for inspection and test tasks [1]. They depend on the lithium batteries and require the regular power replenishment after running for a period of time. At present, the main charging methods for inspection robots are contact charging methods that can be divided into two categories. The first category is regular pluggable charging with artificial maintenance or mechanical automatic control devices. The second category involves sheet metal connected to a power supply that is installed un-insulated on the ground in a charging dock. When the robot moves to a precise position, the sheet metal under the chassis of the robot meets the sheet metal on the ground to start the charging process. There are a number of problems in the contact charging methods mentioned above including contact wear, failed charging connections, inflexible charging and safety issue. These problems are both obvious and pressing. The special tasks for the wireless charging systems of inspection robots include decreasing the requirements of precise parking and charging positions, avoiding exposure to electrical connectors, and satisfying the power rate of charging. To overcome the limitations of traditional charging methods, this paper proposes and investigates a wireless charging system for inspection robots based on a three-phase class-D resonant inverter and its control strategy.

Wireless power transmission (WPT) technology was first proposed by Nicola Tesla in the 1890's and it has been developed substantially over the last two decades. Theoretical research on WPT focuses mainly on high frequency inverters [2], energy couplers [3], [4], compensation circuits [5], impedance matching

Manuscript received Oct. 26, 2018; accepted Feb. 23, 2019
Recommended for publication by Associate Editor Fuxin Liu.
[†]Corresponding Author: xlhuang@seu.edu.cn
Tel: +86-25-83793705, Southeast University
[*]School of Electrical Engineering, Southeast University, China
[**]Key Laboratory of Smart Grid Technology and Equipment in Jiangsu Province, China
[***]Department of Electrical and Computer Engineering, NYU Tandon School of Engineering, USA

[6], and system control [7]-[9]. With the deepening of theoretical research, WPT is finding wide applications including consumer electronics [10], implant medical equipment [11], electric vehicles [12] and rail transit systems [13]. The application of WPT in the charging systems of inspection robots is beneficial to improving charging convenience and safety in addition to further promoting the intelligence of the whole system.

In research on the power control of WPT systems, adjusting the frequency of the inverter to change the system operation frequency is investigated to control the receiving power on the secondary side [14]. However, a wide range frequency adjustment significantly influences the system efficiency in WPT systems. The adjustment control for the DC input voltage of a high frequency inverter is directly applied to changing the receiving power on the secondary side [15]. In this method, the DC-DC converter unit depends on an additional power stage and control circuit which results in extra power loss in the whole system. In [16], the phase-shift method of a multi-phase resonant inverter (MPRI) with a cascaded coupled inductance (CCI) structure is proposed to control the output power of an inverter without adding a DC-DC converter or widely shifting the operation frequency. Cascaded coupled inductances have been used to automatically balance the currents in each phase [17]. The coupled inductances are also called intercell transformers (ICTs) [18]. The multiphase resonant inverter (MPRI) is a new branch of the inverters for the wireless power transfer systems and they have a lot of potential. Output power can also be controlled without a DC-DC converter in the input side. In addition, a higher power rate can be realized by using devices with a lower rated current and a lower price according to this topology.

The parameters in the SS compensation structure are designed without taking the inductances into consideration. Hence, the operation frequency is kept between 83 kHz and 88 kHz according to the TABLE I in [17]. In [19], blocking capacitors are applied and connected after the ICTs in each phase to compensate for the voltage drop caused by the leakage inductance of the ICTs. The leakage inductances in the ICTs are handled independently of the compensation circuit of the primary coil. In this paper, the leakage inductances in the equivalent circuit of the MPRI with a CCI are separated out and reused in the primary compensation circuit. The novel inductance-capacitance-capacitance (LCC) structure combined with the CCI structure in the primary side is presented, and a parameter correction method of the compensation circuit is proposed. The LCC compensation circuit on the primary side is advantageous in preventing the over current caused by a tiny reflected impedance when the coupling between the primary side and the secondary side is too weak [20].

In the WPT systems for mobile power consumption equipment such as inspection robots, several extra auxiliary technologies are applied to estimate whether the secondary side is in the right charging position [1]. The positioning methods are proposed by measuring the voltage / current in the secondary side in [21] and [22]. In this paper, the dynamic characteristics that vary with the relative position of secondary coil are analyzed. The adaptive location scheme during the access and exit processes of moving robots is further investigated. Based on the output voltage control method and the adaptive location scheme, a transition control strategy for the standby and operation modes of the wireless charging systems of inspection robots is put forward in this paper. The standby and operation modes are adaptively conversed without auxiliary positioning technology or an external communication method.

A wireless charging scheme for inspection robots is introduced and a transition control strategy of the standby and operation modes during the access and exit processes of the robot is proposed in this paper. In Section II, the structure of a wireless charging system for inspection robots based on a three-phase class-D resonant inverter is presented. In Section III, a WPT system with a compound compensation circuit and a WPT system with a three-phase class-D resonant inverter are modeled. An output voltage control method based on the equally-spread regulation of the phase difference between adjacent phases is proposed. Additionally, a parameter correction method in the primary compound compensation circuit is put forward. In Section IV, variations of the dynamic characteristics with the relative position of the secondary coil are discussed according to the calculation for the mutual inductance between non-coaxial rectangular spiral coils. In Section V, the adaptive location scheme during the access and exit processes of moving robots is investigated. A transition control strategy for the standby and operation modes of a wireless charging system for inspection robots is proposed by combining the output voltage control method and the adaptive location scheme. Theoretical analyses are verified in Section VI and some conclusions are provided in Section VII.

II. Structure of a Wireless Charging System for Inspection Robots

In order to alleviate existing issues with the charging of inspection robots, a wireless charging system based on a three-phase class-D resonant inverter and a novel compound compensation circuit with ICTs is proposed in this section. As shown in Fig. 1(a), a wireless charging point is set on the inspection routine. The inspection robot moves to the charging point when the battery is low or when the robot is waiting for the next inspection task. The robot exits the charging system and continues its work when the battery is charged or the next inspection task orders arrive. In addition, to take full advantage of the time during stationary inspections, wireless charging points can be installed at positions where the time spent on an

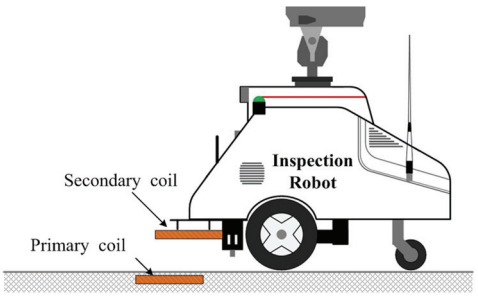

(a)

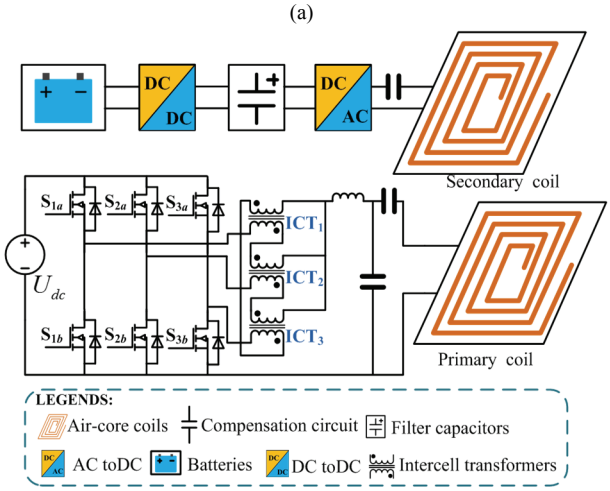

(b)

Fig. 1. Diagrams showing. (a) Schematic of a wireless charging system for an inspection robot. (b) Structure of a wireless charging system with a three-phase class-D resonant inverter.

inspection task is long.

A structure diagram of a wireless charging system with a three-phase Class-D resonant inverter is shown in Fig. 1(b). Rectangular spiral coils are selected as WPT components. The primary side of this system consists of a DC voltage source (U_{dc}), a three-phase class-D resonant inverter, a primary compensation circuit, and a primary coil. The secondary side includes a secondary coil, a secondary compensation circuit, a full-bridge rectifier circuit, a DC filter circuit, a DC-DC converter, and a battery load. In this paper, the three-phase class-D resonant inverter is composed of three paralleled class-D circuits and cascaded ICTs. A novel LCC topology combined with cascaded ICTs is applied as the primary compensation circuit in this paper. On the one hand, the ICTs are applied to balance the currents in each of the phases [17]. On the other hand, the ICTs are a part of the primary compensation circuit. An inductance-capacitor (LC) series connection is selected as the compensation circuit in the secondary side. When the inspection robot moves to the charging position, energy can be transferred wirelessly through magnetic coupling between the primary side (the coil on the ground) and the secondary side (the coil under the chassis). This paper focuses on the transition control strategy of the standby and operation modes. Hence, several parts including the full-bridge rectifier circuit, the DC filter circuit, the DC-DC converter, and the battery load in the secondary side are equivalent to an AC load resistance, which has been discussed in [1].

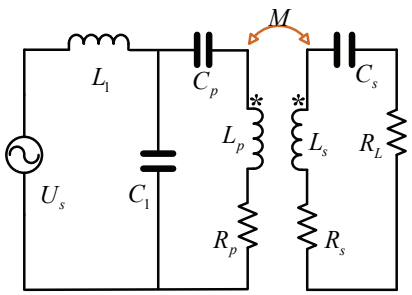

Fig. 2. Equivalent circuit of a WPT system with the LCC compensation topology in the primary side.

III. Circuit Analysis and Modeling

A. Modeling of a Traditional WPT System with LCC Compensation in the Primary Side

The WPT system consists of a high frequency source, a primary compensation circuit, a primary coil, a secondary coil, a secondary compensation circuit, and a load. The equivalent circuit of the WPT system with the LCC compensation topology in the primary side and the LC compensation topology in the secondary side is shown in Fig. 2, where U_s is the output voltage of the inverter, L_p and L_s represent the inductances of the primary and secondary coil, and R_p and R_s denote the internal resistances of the primary and secondary coil, respectively. The inductance L_1, and the capacitors C_1 and C_p make up the compound compensation circuit in the primary side. C_s is the serial compensation capacitor in the secondary side, R_L is the load, and M indicates the mutual inductance between the primary and secondary coil.

In Fig. 2, the series compensation topology is applied in the secondary side. To realize the resonance in the secondary side and achieve a higher secondary current, the compensation capacitor C_s should satisfy:

$$C_s L_s = \frac{1}{\omega^2} \tag{1}$$

where $\omega = 2\pi f$, and f is the operating frequency.

The reflected impedance Z_r from the secondary side to the primary side is:

$$Z_r = \frac{(\omega M)^2}{R_L + R_s} \tag{2}$$

The total impedance Z_{in} after the high-frequency power source is expressed by:

$$Z_{in} = j\omega L_1 + \frac{\left(\frac{1}{j\omega C_p} + j\omega L_p + R_p + Z_r\right)\frac{1}{j\omega C_1}}{\frac{1}{j\omega C_1} + \frac{1}{j\omega C_p} + j\omega L_p + R_p + Z_r} \tag{3}$$

In a WPT system with an LCC compensation circuit in the primary side, in order to maintain a stable current in the primary coil [1], the inductance and capacitances in the primary compensation circuit should meet the following conditions:

$$C_1 L_1 = \frac{1}{\omega^2}, C_p\left(L_p - L_1\right) = \frac{1}{\omega^2} \tag{4}$$

(3) is simplified as:

$$Z_{in} = \frac{\omega^2 L_1^{\,2}}{R_p + Z_r} \tag{5}$$

The output current of the inverter is:

$$\begin{aligned} I_f &= \frac{U_s}{Z_{in}} = \frac{U_{in}\left(R_p + Z_r\right)}{\omega^2 L_1^{\,2}} \\ &= \frac{U_s\left(R_p\left(R_s + R_L\right) + \left(\omega M\right)^2\right)}{\omega^2 L_1^{\,2}\left(R_s + R_L\right)} \end{aligned} \tag{6}$$

The primary current in the primary coil can be represented as:

$$\begin{aligned} I_p &= \frac{U_s\left(R_p + Z_r\right)}{\omega^2 L_1^{\,2}} \bullet \frac{\left(\dfrac{1}{j\omega C_p} + j\omega L_p + R_p + Z_r\right)\dfrac{1}{j\omega C_1}}{\dfrac{1}{j\omega C_1} + \dfrac{1}{j\omega C_p} + j\omega L_p + R_p + Z_r} \\ &\bullet \frac{1}{\dfrac{1}{j\omega C_p} + j\omega L_p + R_p + Z_r} \\ &= \frac{U_s}{j\omega L_1} \end{aligned} \tag{7}$$

According to the mutual inductance theory, the current of the secondary coil is:

$$I_s = \frac{j\omega M I_p}{R_L + R_s} = \frac{M U_s}{L_1\left(R_L + R_s\right)} \tag{8}$$

The receiving power of load in the secondary is:

$$P = I_s^{\,2} R_L = \frac{M^2 U_s^{\,2} R_L}{L_1^{\,2}\left(R_L + R_s\right)^2}. \tag{9}$$

The power loss in the whole system can be expressed as:

$$P_{loss} = I_p^{\,2} R_p + I_s^{\,2} R_s = \frac{U_s^{\,2}}{L_1^{\,2}}\left(\frac{R_p}{\omega^2} + \frac{M^2 R_s}{\left(R_L + R_s\right)^2}\right). \tag{10}$$

B. Modeling of a Three-phase Class-D Resonant Inverter

A three-phase class-D resonant inverter with cascaded ICTs, as shown in Fig. 3, is adopted as the power source in this paper, where U_{dc} is the DC input voltage of the inverter. MOSFETs (S_{1a}/S_{1b}, S_{2a}/S_{2b} and S_{3a}/S_{3b}) comprise the three class-D circuits in this inverter. U_1, U_2 and U_3 represent the fundamental component of the square wave output voltage of each phase. The currents of three phases are denoted as I_1, I_2 and I_3 respectively. ICT_1, ICT_2 and ICT_3 indicate the cascaded ICTs. L_{ICT1p}, L_{ICT2p}, and L_{ICT3p} are the primary side

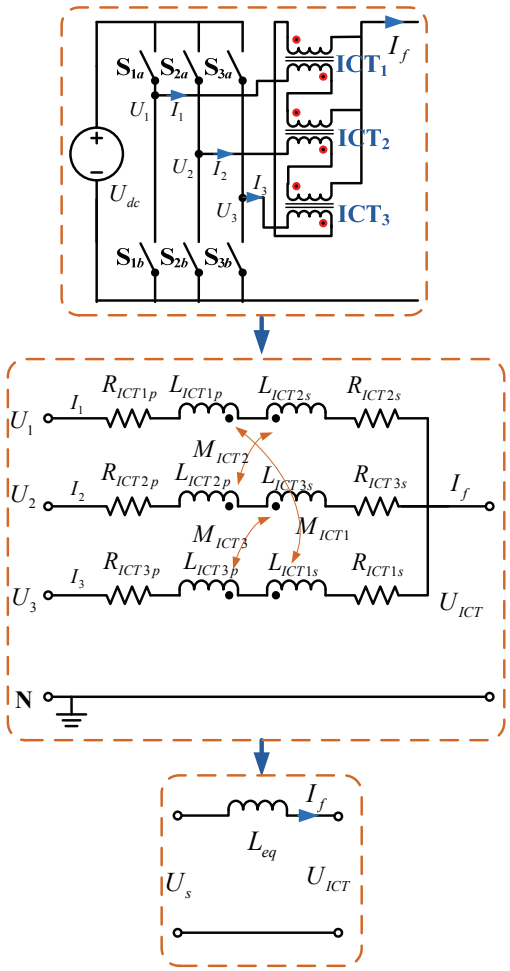

Fig. 3. Circuit topology and equivalent single-phase circuit of a three-phase class-D resonant inverter.

inductances for each of the ICTs. L_{ICT1s}, L_{ICT2s} and L_{ICT3s} are the secondary side inductances for each of the ICTs. M_{ICT1}, M_{ICT2} and M_{ICT3} are the mutual inductances between the primary and secondary side in ICTs. The tiny internal resistances of the ICTs windings are ignored in this paper.

As shown in Fig. 3, U_{ICT} is the output voltage after the cascaded ICTs. The following equations can be established according to the circuit theory:

$$\begin{cases} U_1 = \left(j\omega L_{ICT1p} + j\omega L_{ICT2s}\right) I_1 - j\omega M_{ICT1} I_3 \\ \qquad - j\omega M_{ICT2} I_2 + U_{ICT} \\ U_2 = \left(j\omega L_{ICT2p} + j\omega L_{ICT3s}\right) I_2 - j\omega M_{ICT2} I_1 \\ \qquad - j\omega M_{ICT3} I_3 + U_{ICT} \\ U_3 = \left(j\omega L_{ICT3p} + j\omega L_{ICT1s}\right) I_3 - j\omega M_{ICT3} I_2 \\ \qquad - j\omega M_{ICT1} I_1 + U_{ICT} \\ I_f = \sum_{i=1}^{3} I_i \end{cases} \tag{11}$$

where U_s is the output voltage of the three-phase class-D resonant inverter in the equivalent single-phase circuit.

Assuming that the inductances for each of the windings in the ICTs are equal, which can be represented as L_{ICT}, and that the mutual inductances for each of the ICTs are equal, which can be denoted as M_{ICT}, (11) can be written as:

$$U_s = \frac{1}{3}\sum_{i=1}^{3} U_i = \frac{2}{3} j\omega\left(L_{ICT} - M_{ICT}\right) I_f + U_{ICT} \tag{12}$$

C. Output Voltage Control Method

According to (12), the output voltage of a three-phase class-D resonant inverter can be equal to a single-phase voltage source. In this paper, three phases are designed to be equally spread with the phase differences between adjacent phases denoted as $\delta\left[0^\circ, 120^\circ\right]$. The voltages for each of the phases in the phasor form are expressed as:

$$U_1 = \frac{2}{\pi} U_{dc} \angle(\delta), U_2 = \frac{2}{\pi} U_{dc} \angle(0), U_3 = \frac{2}{\pi} U_{dc} \angle(-\delta). \tag{13}$$

Hence, (12) is equal to:

$$\begin{aligned} U_s &= \frac{1}{3}\sum_{i=1}^{3} U_i \\ &= \frac{1}{3}\pi\left(\frac{2}{\pi} U_{dc}\angle(\delta) + \frac{2}{\pi} U_{dc}\angle(0) + \frac{2}{\pi} U_{dc}\angle(-\delta)\right) \\ &= \frac{2}{3\pi} U_{dc}\left(\cos(\delta) + j\sin(\delta) + 1 + \cos(\delta) - j\sin(\delta)\right) \\ &= \frac{2}{3\pi} U_{dc}\left(1 + 2\cos(\delta)\right)\angle(0) \end{aligned} \tag{14}$$

Based on (15), equivalent output voltage control can be realized by adjusting δ. An output voltage control method based on the equally-spread regulation of the phase difference between adjacent phases is proposed to lay the foundation for receiving the power control demand in later sections.

D. Parameter Correction Method in the Primary Side

According to (12), the serial inductance after the equivalent single-phase source can be express as:

$$L_{ICT}' = \frac{2}{3}\left(L_{ICT} - M_{ICT}\right). \tag{15}$$

In order to maintain the design of L_1 in the equivalent circuit of a WPT system with the LCC compensation topology in the primary, side as shown in Fig. 2, the actual value of the inductance in the compound compensation circuit should be corrected. The parameter correction value of L_1 is expressed as:

$$L_{1corr} = L_1 - L_{ICT}'. \tag{16}$$

To achieve the total inductance L_1, the actual value of this inductance should be selected according to (16) when designing the compensation circuits in the WPT system.

IV. System Characteristics Analysis

The primary and secondary coils in the wireless charging system for inspection robots are rectangular spiral coils. In the primary coil, the maximum length is L and the maximum width is W. The number of turns of the primary coil is N_1. In the secondary coil, the maximum length is l and the maximum width is w. The number of turns of the primary coil is N_2. The distance between the adjacent turns of every coil is d.

The i^{th} loop in the primary coil is $\boldsymbol{l}_{p(i)}$. The j^{th} loop in the secondary coil is $\boldsymbol{l}_{s(j)}$. Hence, the mutual inductance between the i^{th} loop in the primary coil and the j^{th} loop in the secondary coil can be expressed as:

$$M_{ij} = \frac{\mu_r \mu_0}{4\pi} \int_{l_{p(i)}} \int_{l_{s(j)}} \frac{\mathrm{d}\boldsymbol{l}_{p(i)} \bullet \mathrm{d}\boldsymbol{l}_{s(j)}}{R_{ij}} \tag{17}$$

where μ_r is the relative magnetic permeability ($\mu_r \approx 1$, in air), μ_0 is the magnetic permeability of vacuum ($\mu_0 = 4\pi \times 10^{-7}$ H/m), and R_{ij} represents the distance between the current microelements of the i^{th} loop in the primary coil and of the j^{th} loop in the secondary coil.

The total mutual inductance between non-coaxial rectangular spiral coils can be calculated according to:

$$M = \left|\sum_{i=1}^{N_1}\sum_{j=1}^{N_2} M_{ij}\right| = \left|\sum_{i=1}^{N_1}\sum_{j=1}^{N_2} \frac{\mu_r \mu_0}{4\pi} \int_{l_{p(i)}} \int_{l_{s(j)}} \frac{\mathrm{d}\boldsymbol{l}_{p(i)} \bullet \mathrm{d}\boldsymbol{l}_{s(j)}}{R_{ij}}\right|. \tag{18}$$

In this paper, the primary and secondary coils are designed the same. The length is $L = l = 0.30$ m. The width is $W = w = 0.30$ m. The number of turns is $N_1 = N_2 = 7$. The vertical height between the primary and secondary coils is $h = 0.08$ m. The distance between the adjacent turns of every coil d is 0.01 m. The inspection robot usually runs along a fixed line. It is assumed that the robot moves in the direction of the x axis without misalignment in other directions. The coordinate value in the x axis (O_x) of the center of the secondary coil is changed to replace the moving process of the inspection robot. The variation range of O_x is set as $O_x \in \left[-1.5w, 1.5w\right]$ ($O_x \in \left[-0.45, 0.45\right]$).

The variation characteristics of several key system parameters are considered under different input voltage conditions in diverse system modes. By changing δ to adjust the output voltage of an inverter based on (14), the equivalent single-phase output voltage U_{eq1} in the standby mode and U_{eq2} ($U_{eq1} < U_{eq2}$) in the operation mode can be obtained. According to (18) and (3), when O_x is changed between -1.5w and 1.5w, the comparative characteristics of the normalized output current I_f of a three-phase class-D resonant inverter varying with the position change of the secondary coil under different system voltages is shown in Fig. 4.

According to (9), (10) and (18), the comparative characteristics of the normalized receiving power and the normalized power loss varying with position changes of the secondary coil under different system voltages can be obtained as shown in Fig. 5.

In Fig. 5, if the system is in the standby mode (lower input voltage), the receiving power is low even when there is no

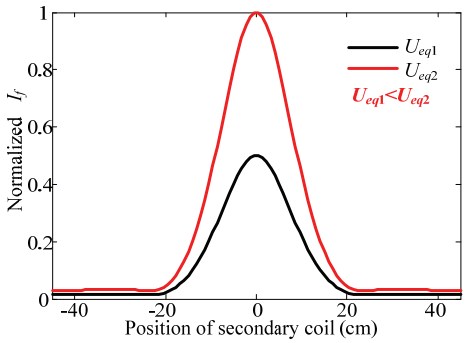

Fig. 4. Comparative characteristics of the normalized output current I_f varying with position changes of the secondary coil under different system voltages.

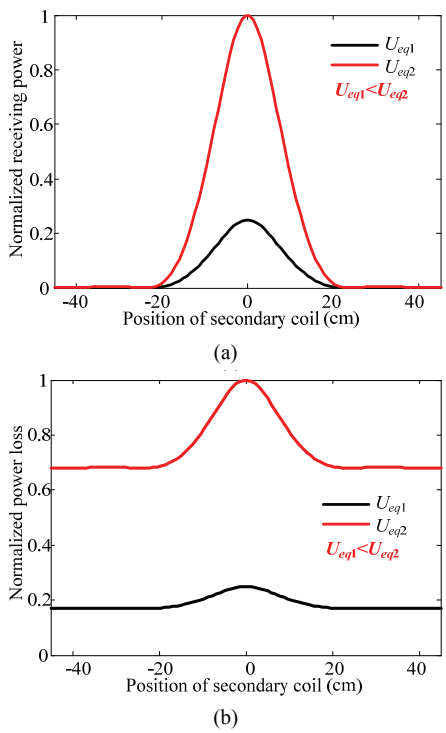

Fig. 5. Comparative characteristics. (a) Normalized receiving power. (b) Normalized power loss.

misalignment between the primary and secondary coils. It is difficult to satisfy the charging requirements of an inspection robot. On the other hand, it is remarkable that the power loss is low when the secondary coil is far away from the primary coil in the standby mode. If the system is in the operation mode (higher input voltage), the receiving power is high when the secondary coil is close to the primary coil. However, the power loss is still high when the secondary coil is far from the primary coil in the operation mode. In the next section, taking the variation characteristics shown in Fig. 4 and Fig. 5 into consideration, the adaptive location scheme during the access and exit processes of a moving robot, and the transition control strategy of the standby and operation modes is further discussed.

V. Transition Control Strategy of the Standby and Operation Modes

Based on the output voltage control method with equally-spread regulation of the phase difference between adjacent phases in (14), the output voltages U_{eq1} and U_{eq2} can be obtained by directly setting δ . The phase difference corresponding to U_{eq1} is represented by δ_1 , while the phase difference corresponding to U_{eq2} is represented by δ_2 .

To select the transition positions of the standby and operation modes, the adaptive location scheme during the access and exit processes of moving robots is proposed. When the secondary coil is far from the primary coil, the system is in the standby mode. In this mode, the mutual inductance is tiny and the system efficiency is low. During the access process of an inspection robot, with the misalignment between the primary and secondary coils shortening, the output current of the inverter I_f increases rapidly near the non-misalignment position. Hence, I_f is identified as the discrimination information of the position to distinguish the access transition point (O_1) from the standby mode to the operation mode. The access transition point is set at the position where I_f reaches I_{f1}. In greater detail, when I_f is found to be higher than I_{f1}, the standby mode is converted to the operation mode. After this transition control, the output current of the inverter I_f is I_{f1}' in the operation mode.

In the exit process of an inspection robot, the receiving power and I_f are decreased due to the fact that the misalignment between the primary and secondary coils increases. When the receiving power is too low, the system mode should be converted from the operation mode to the standby mode to decrease the power loss of the whole system. Hence, the position where I_f reaches I_{f2} is selected as the exit transition point (O_2) to realize the transition control from the operation mode to the standby mode. The whole variation process of I_f in the transition control is shown in Fig. 6. When I_f is found to be lower than I_{f2} in the operation mode, the system mode is converted to the standby mode. After the transition control, the output current of inverter I_f is I_{f2}' in the standby mode.

It is remarkable that if $I_{f1}' \le I_{f2}$ or $I_{f2}' \ge I_{f1}$, the system runs into an endless loop between the standby mode and the operation mode. Hence, the selection of the transition points in the transition control strategy should satisfy that $I_{f1}' > I_{f2}$ and $I_{f2}' < I_{f1}$. As shown in Fig. 6, the variation characteristic of the output current I_f varying with the position change of the secondary coil is symmetrical. Thus, O is closer to the access transition point (O_1) than the exit transition point (O_2).

Based on the output voltage control method and the adaptive location scheme, a transition control strategy of the standby and operation modes of a wireless charging system for inspection robots is proposed. A flow chart of the transition

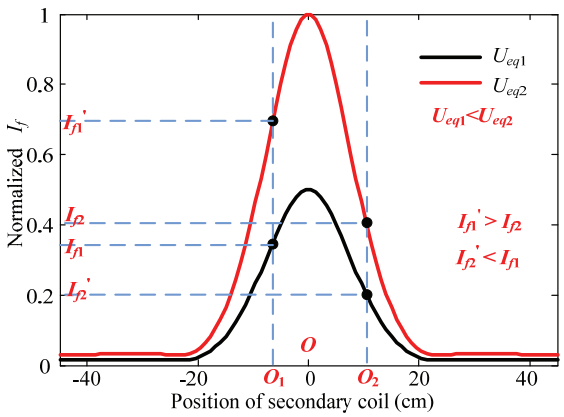

Fig. 6. Whole variation process of I_f in the transition control.

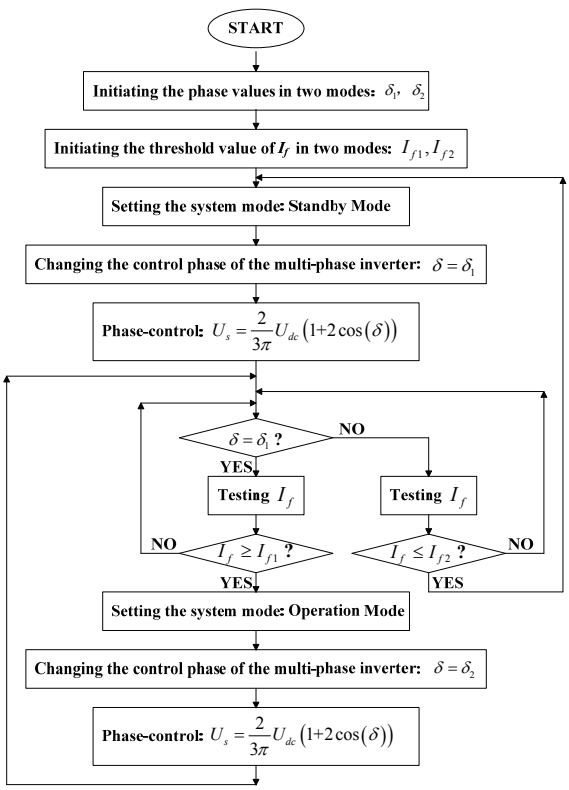

Fig. 7. Flow chart of the transition control strategy.

control strategy is shown in Fig. 7.

The preset values in the transition control strategy are initiated first. The phase differences between the adjacent phases of the standby mode and the operation mode are set as δ_1 and δ_2, respectively. The threshold values of the inverter output current I_f of the standby mode and the operation mode are set as I_{f1} and I_{f2}, respectively. Then the system mode is set as the standby mode, and the phase difference is set to be $\delta = \delta_1$ to control the output voltage of the inverter in the standby mode. When $\delta = \delta_1$ (the standby mode), the system mode should be converted to the operation mode if $I_f \geq I_{f1}$. The phase difference is set to be $\delta = \delta_2$ to control the output voltage of the inverter for the operation mode. When $\delta = \delta_2$ (the operation mode), the system mode should be converted to the standby mode if $I_f \leq I_{f2}$. The phase difference is set to be $\delta = \delta_1$ to control the output voltage of the inverter for the standby mode. According to the transition control strategy, the system mode can be adaptively converted between the standby mode and the operation mode. The system characteristics including the high receiving power in the operation mode and the low power loss in the standby mode can be realized without auxiliary positioning technology or external communication systems.

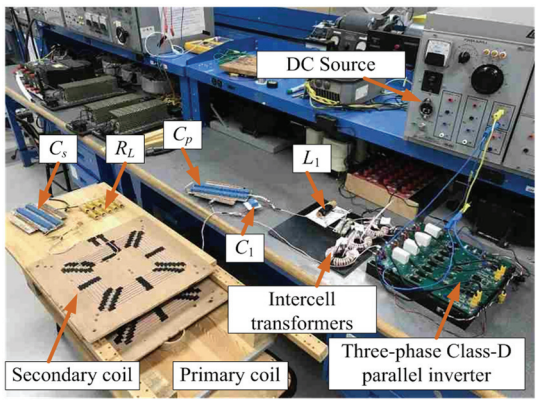

Fig. 8. Experimental prototype of a wireless power transfer system.

VI. Experimental Verification

An experimental prototype of the wireless power transfer system was built in the laboratory as shown in Fig. 8. The three-phase class-D inverter is controlled by a micro controller (STM32F407VGT) and a field-programmable gate array (XC6SLX9). MOSFETs (IRFP4227) are selected as the switching devices in the power stage of the inverter. The ICTs are made with the core and litz wire. The system is designed to work at 85 kHz. Each of the ICTs contains two identical windings in which the number of turns is 30. The inductance of the single winding in the ICT is 11.2 μH. The mutual inductance between the two windings of the ICT is 10.3 μH.

The primary and secondary coils are made from litz wire. They are designed identically according to the parameters in the theoretical analysis. The inductance and the internal resistance of the primary and secondary coils are 20.1 μH and 60 mΩ, respectively. In order to design L_1=5.0 μH in the primary compound compensation circuit, according to (16), the actual value of L_{1corr} should be selected as 4.4 μH. Based on (1) and (4), C_1 is 700.5 nF (the calculated value is 701.2 nF) and C_p is 231.7 nF (the calculated value is 232.2 nF). Cs is 173.6 nF (the calculated value is 174.4 nF). The load resistance is 4.2 Ω.

The RMS value of the output voltage of each phase in the three-phase class-D resonant inverter is 20 V according to the

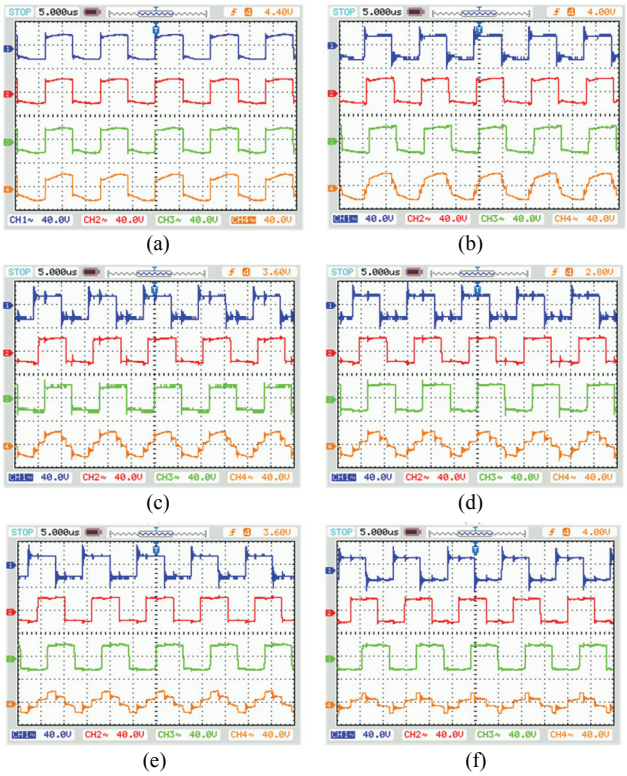

Fig. 9. Waveforms of the output voltage of the inverter under different phase differences δ . U_1(40 V/div), U_2(40 V/div), U_3(40 V/div) and U_s(40 V/div). (a) δ=0° , U_s=19.8 V. (b) δ=15.4° , U_s=19.3 V. (c) δ=30.7° , U_s=17.8 V. (d) δ=46.0° , U_s=15.5 V. (e) δ=61.4° , U_s=12.8 V. (*f*) δ=76.7° , U_s=9.7 V.

constant DC source. In order to verify the output voltage control method based on the equally-spread regulation of the phase difference between adjacent phases, the phase difference δ is changed. The output voltage of the three-phase class-D resonant inverter is tested by using a digital oscilloscope (RIGOL DS1074B) and a differential probe (PROBE MASTER Model 4231). Waveforms of the output voltage of the inverter under different phase differences δ are shown in Fig. 9. The output voltage of the inverter varying with the different phase differences δ is shown in Fig. 10.

According to the control characteristic shown in Fig. 10, the output voltage in the standby mode is selected as U_s=9.7 V by setting $\delta=\delta_2$=76.7° , and the output voltage in the operation mode is selected as U_s=19.8 V by setting $\delta=\delta_1$=0° .

The output current I_f is detected by using a current transformer manufactured with a 25 mm-diameter ferrite core. The turns ratio of the current transformer is 1:50. High frequency current is converted to high frequency voltage across the resistance which is connected to the current transformer. After the proportional amplification circuit, precision rectifier circuit and voltage divider circuit, this high frequency voltage is further converted to DC voltage $U_{DC\text{-}If}$. The proportional relationship between the DC voltage $U_{DC\text{-}If}$ (V) and the current I_f (A) is 9:70. The variation characteristic

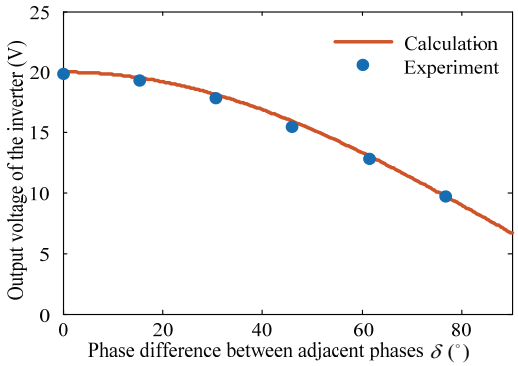

Fig. 10. Output voltage of an inverter varying with different phase differences δ .

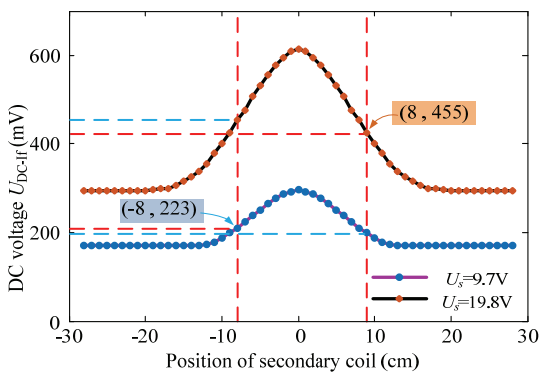

Fig. 11. Comparative variation characteristics of $U_{DC\text{-}If}$ varying with the position of the secondary coil.

of $U_{DC\text{-}If}$ is measured by an ADC (analog-digital conversion) module in the microcontroller. The DC voltage $U_{DC\text{-}If}$ is measured at different positions of the secondary coil in the standby and operation modes. The comparative variation characteristics of $U_{DC\text{-}If}$, varying with the position of the secondary coil in different modes, are shown in Fig. 11.

According to the comparative results shown in Fig. 11, $U_{DC\text{-}If1}$ and $U_{DC\text{-}If2}$ are considered to represent I_{f1} and I_{f2} in the proposed adaptive location scheme. $U_{DC\text{-}If1}$ is set to 225 mV (slightly higher than 223 mV) as the access transition point in the standby mode. $U_{DC\text{-}If2}$ is set to 450 mV (slightly lower than 455 mV) as the exit transition point in the operation mode. $U_{DC\text{-}If1}$ and $U_{DC\text{-}If2}$ satisfy the conditions to avoid the endless loop between the standby mode and operation mode.

After changing the position of the secondary coil, the receiving power and total power in the primary side are obtained in the standby and operation modes. The comparative characteristics of the receiving power and total power in the primary side varying with the secondary coil position when U_s=19.8 V and U_s=9.7 V are shown in Fig. 12(a). Under a higher voltage (U_s=19.8 V), the receiving power is high when the secondary coil is at small misalignment positions and the total power in the primary side is significantly high even when the secondary coil is at large misalignment positions. Under a lower voltage (U_s=9.7 V), the total power in the primary side is low when the

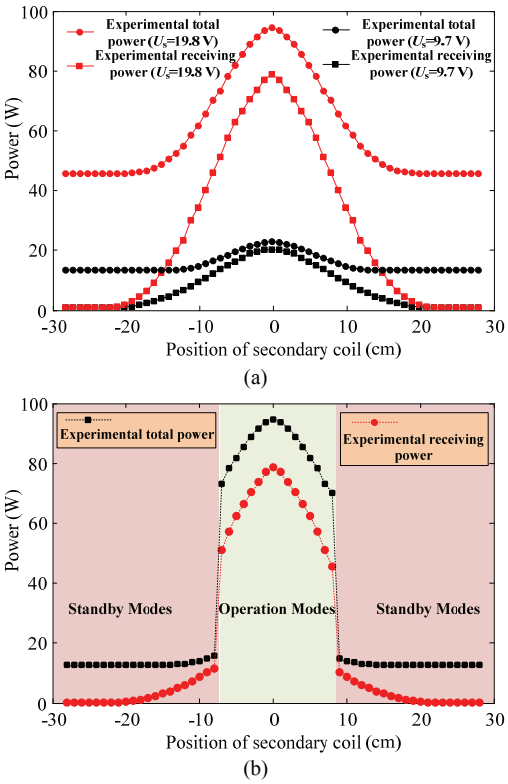

Fig. 12. Comparative characteristics. (a) The receiving power and total power in the primary side varying with the secondary coil position when U_s=19.8 V and U_s=9.7 V. (b) The receiving power and total power in the primary side varying with the secondary coil position when the transition control strategy is applied.

secondary coil is at large misalignment positions and the receiving power is significantly low even when the secondary coil is at small misalignment positions.

Based on the transition control strategy of the standby and operation modes proposed in this paper, the system mode is set to the standby mode ($\delta=\delta_2=76.7^\circ$ and U_s=9.7 V) when the secondary side is far from the primary side. During the access process of an inspection robot, $U_{DC\text{-}If}$ increases when the secondary coil moves closer to the primary coil in the standby mode. If $U_{DC\text{-}If} > U_{DC\text{-}If1}$, the system mode should be converted to the operation mode. The phase difference δ is set to $\delta=\delta_1=0^\circ$ to achieve U_s=19.8 V. During the exit process of an inspection robot, $U_{DC\text{-}If}$ decreases when the secondary coil moves further from the primary coil in the standby mode. If $U_{DC\text{-}If} < U_{DC\text{-}If2}$, the system mode should be converted to the standby mode. The phase difference δ is set to $\delta=\delta_2=76.7^\circ$ to obtain U_s=9.7 V. The comparative characteristics of the receiving power and total power in primary side varying with the secondary coil position when the transition control strategy is applied are shown in Fig. 12(b).

On the basis of the transition control strategy, including the voltage adjustment method and the adaptive location scheme, the system mode automatically transits between the standby mode and the operation mode without an external communication method or auxiliary positioning technology. In the standby mode, the total power in the primary side is low. Specifically, the standby power is 12.8 W when the inspection robot is far from the primary coil. The maximum standby power is 16.8 W in the whole process. In the operation mode, the highest receiving power is 80.6 W and the efficiency is 85.2% when the misalignment between the primary coil and the secondary coil is zero. When compared to a system working under a fixed source voltage, the system characteristics including the low standby power in the standby mode and the high receiving power in the operation mode are realized when the transition control strategy is applied.

VII. Conclusion

A wireless charging system for inspection robots based on a three-phase class-D resonant inverter is introduced in this paper to solve the problems of contact charging methods. The main emphasis of this paper is the transition control strategy for this system. Relevant experiments are designed to verify the theoretical analyses. The conclusions are drawn as follows.

(1) A three-phase class-D resonant inverter is applied in a wireless charging system with a novel LCC compensation circuit in the primary side. An output voltage control method based on equally-spread regulation of the phase difference between adjacent phases is proposed. A parameter correction method in the primary side when the cascaded ICTs are taken into consideration is presented.

(2) The dynamic characteristics of the system varying with the relative position of the secondary coil during the access and exit processes of a moving robot are investigated according to the calculation of the mutual inductance between non-coaxial rectangular spiral coils.

(3) According to the current variation characteristic, the adaptive location scheme during the access and exit processes of a moving robot is investigated without an external communication method or auxiliary positioning technology.

(4) Combining the output voltage control method and the adaptive location scheme, a transition control strategy of the standby and operation modes is presented to realize a number of system characteristics including the a standby power in the standby mode and a high receiving power in the operation mode. The proposed transition control strategy is also helpful when it comes to the switching control in dynamic wireless charging systems with short-segmented coils.

Acknowledgment

This work was supported in part by State Grid Corporation Science and Technology Project Funding (Selection of Wireless Charging Frequency for Electric Vehicles and Its Impact on Environment), in part by the Science and Technology Project of China State Grid Corporation (Research on the Application

of Electromagnetic Metamaterials in Improving Transmission Efficiency and Electromagnetic Shielding Performance of WPT Systems), in part by National key R & D project (NO.2018 YFB0106300), in part by the National Natural Science Foundation of China (51877036), in part by the Scientific Research Foundation of Graduate School of Southeast University (YBJJ1728) and in part by the Postgraduate Research & Practice Innovation Program of Jiangsu Province (KYCX17-0088). This work was also supported by the China Scholarship Council.

REFERENCES

[1] H. Liu, X. Huang, L. Tan, J. Guo, W. Wang, C. Yan, and C. Xu, "Dynamic wireless charging for inspection robots based on decentralized energy pickup structure," *IEEE Trans. Ind. Informat.*, Vol. 14, No. 4, pp. 1786-1797, Apr. 2018.

[2] J. Choi, D. Tsukiyama, Y. Tsuruda, and J. M. R. Davila, "High-frequency, high-power resonant inverter with eGaN FET for wireless power transfer," *IEEE Trans. Power Electron.*, Vol. 33, No. 3, pp. 1890-1896, Mar. 2018.

[3] C. K. Lee, W. X. Zhong, and S. Y. R. Hui, "Effects of magnetic coupling of nonadjacent resonators on wireless power domino-resonator systems," *IEEE Trans. Power Electron.*, Vol. 27, No. 4, pp. 1905-1916, Apr. 2012.

[4] Y. Wang, Y. Yao, X. Liu, D. Xu, and L. Cai, "An LC/S compensation topology and coil design technique for wireless power transfer," *IEEE Trans. Power Electron.*, Vol. 33, No. 3, pp. 2007-2025, Mar. 2018.

[5] F. Lu, H. Zhang, H. Hofmann, and C. C. Mi, "An inductive and capacitive integrated coupler and its LCL compensation circuit design for wireless power transfer," *IEEE Trans. Ind. Appl.*, Vol. 53, No. 5, pp. 4903-4913, Sep./Oct. 2017.

[6] J. Lim, B. Lee, and M. Ghovanloo, "Optimal design of a resonance-based voltage boosting rectifier for wireless power transmission," *IEEE Trans. Ind. Electron.*, Vol. 65, No. 2, pp. 1645-1654, Feb. 2018.

[7] W. Zhong and S. Y. R. Hui, "Auxiliary circuits for power flow control in multifrequency wireless power transfer systems with multiple receivers," *IEEE Trans. Power Electron.*, Vol. 30, No. 10, pp. 5902-5910, Oct. 2015.

[8] Y. Zhang, T. Lu, Z. Zhao, F. He, K. Chen, and L. Yuan, "Selective wireless power transfer to multiple loads using receivers of different resonant frequencies," *IEEE Trans. Power Electron.*, Vol. 30, No. 11, pp. 6001-6005, Nov. 2015.

[9] H. Liu, L. Tan, X. Huang, C. Yan, J. Guo, and W. Wang, "Primary topology selection and conversion in short-segmented on-road charging system for electrical vehicles," *IET Power Electron.*, Vol. 10, No. 4, pp. 499-507, Mar. 2017.

[10] H. Hoang, S. Lee, Y. Kim, Y. Choi, and F. Bien, "An adaptive technique to improve wireless power transfer for consumer electronics," *IEEE Trans. Consum. Electron.*, Vol. 58, No. 2, pp. 327-332, May 2012.

[11] R. Das and H. Yoo, "A multiband antenna associating wireless monitoring and nonleaky wireless power transfer system for biomedical implants," *IEEE Trans. Microw. Theory Techn.*, Vol. 65, No. 7, pp. 2485-2495, Jul. 2017.

[12] F. Lu, H. Zhang, and C. Mi, "A two-plate capacitive wireless power transfer system for electric vehicle charging applications," *IEEE Trans. Power Electron.*, Vol. 33, No. 2, pp. 964-969, Feb. 2018.

[13] J. H. Kim, B.-S. Lee, J.-H. Lee, S.-H. Lee, C.-B. Park, S.-M. Jung, S.-G. Lee, K.-P. Yi, and J. Baek, "Development of 1-MW inductive power transfer system for a high-speed train," *IEEE Trans. Ind. Electron.*, Vol. 62, No. 10, pp. 6242-6250, Oct. 2015.

[14] C.-S. Wang, O. H. Stielau, and G. A. Covic, "Design considerations for a contactless electric vehicle battery charger," *IEEE Trans. Ind. Electron.*, Vol. 52, No. 5, pp. 1308-1314, Oct. 2005.

[15] Z. Li, C. Zhu, J. Jiang, K. Song, and G. Wei, "A 3-kW wireless power transfer system for sightseeing car supercapacitor charge," *IEEE Trans. Power Electron.*, Vol. 32, No. 5, pp. 3301-3316, May 2017.

[16] M. Bojarski, E. Asa, K. Colak, and D. Czarkowski, "Analysis and control of multiphase inductively coupled resonant converter for wireless electric vehicle charger applications," *IEEE Trans. Transport. Electrific.*, Vol. 3, No. 2, pp. 312-320, Jun. 2017.

[17] G. J. Capella, J. Pou, S. Ceballos, J. Zaragoza, and V. G. Agelidis, "Current-balancing technique for interleaved voltage source inverters with magnetically coupled legs connected in parallel," *IEEE Trans. Ind. Electron.*, Vol. 62, No. 3, pp. 1335-1344, Mar. 2015.

[18] E. Laboure, A. Cuniere, T. A. Meynard, F. Forest, and E. Sarraute, "A theoretical approach to intercell transformers, application to interleaved converters," *IEEE Trans. Power Electron.*, Vol. 23, No. 1, pp. 464-474, Jan. 2008.

[19] Q. Deng, J. Liu, D. Czarkowski, W. Hu, and H. Zhou, "An inductive power transfer system supplied by a multiphase parallel inverter," *IEEE Trans. Ind. Electron.*, Vol. 64, No. 9, pp. 7039-7048, Sep. 2017.

[20] T. Kan, T. D. Nguyen, J. C. White, R. K. Malhan, and C. C. Mi, "A new integration method for an electric vehicle wireless charging system using LCC compensation topology: analysis and design," *IEEE Trans. Power Electron.*, Vol. 32, No. 2, pp. 1638-1650, Feb. 2017.

[21] H. H. Wu, H. Malek, and M. P. Masquelier, "Determining physical alignment between magnetic couplers for wireless power transfer," U.S. Patent 20150155095, Apr. 6, 2015.

[22] Y. Gao, C. Duan, A. A. Oliveira, A. Ginart, K. B. Farley, and Z. T. H. Tse, "3-D coil positioning based on magnetic sensing for wireless EV charging," *IEEE Trans. Transport. Electrific.*, Vol. 3, No. 3, pp. 578-588, Sep. 2017.

Han Liu was born in Hubei, China, in 1993. He received his B.S. degree from the School of Electrical Engineering, Southeast University, Nanjing, China, in 2014, where he is presently working towards his Ph.D. degree. He was a Visiting Student at New York University, New York, NY, USA, from October 2017 to October 2018. His current research interests include wireless power transfer, dynamic wireless charging applications and high frequency power electronics.

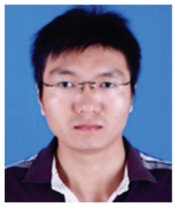

Linlin Tan received his B.S. degree in Electrical Engineering and Automation from the Harbin Engineering University, Harbin, China, in 2008; and his Ph.D. degree in Electrical Engineering from Southeast University, Nanjing, China, in 2014. He is presently working as a Lecturer in the School of Electrical Engineering, Southeast University. Dr. Tan has published more than 20 papers. His current research interests include wireless power transfer, wireless charging for electric vehicles and wireless V2G.

Xueliang Huang received his B.S., M.S. and Ph.D. degrees in Electrical Engineering from Southeast University, Nanjing, China, in 1991, 1994 and 1997, respectively. From 2002 to 2004, he worked as a Post-Doctoral Fellow at the University of Tokyo, Tokyo, Japan. Since 2004, he has been a Professor in the Department of Electrical Engineering, Southeast University. He is the author of four books and more than 150 articles. He is also the creator of more than 40 inventions. His current research interests include wireless power transfer, the analysis of electromagnetic fields, electromagnetic applications, and intelligent electricity technology.

Dariusz Czarkowski received his M.S. degree in Electronics from the AGH University of Science and Technology, Krakow, Poland, in 1989; his M.S. degree in Electrical Engineering from Wright State University, Dayton, OH, USA, in 1993; and his Ph.D. degree in Electrical Engineering from the University of Florida, Gainesville, FL, USA, in 1996. In 1996, he joined the New York University Tandon School of Engineering, Brooklyn, NY, USA, where he is presently working as a Professor of Electrical and Computer Engineering. He is a coauthor of the book *Resonant Power Converters* (Wiley-IEEE Interscience, 2011). His current research interests include power electronics and power distribution systems. He is an Associate Editor of the *International Journal of Power and Energy Systems*.